Available online at www.sciencedirect.com

ScienceDirect

Geochimica et Cosmochimica Acta 121 (2013) 667–683

Geochimica et Cosmochimica Acta

www.elsevier.com/locate/gca

Sorptive fractionation of organic matter and formation of organo-hydroxy-aluminum complexes during litter biodegradation in the presence of gibbsite

K. Heckman [a,b,*], A.S. Grandy [c,1], X. Gao [d,2], M. Keiluweit [e,3], K. Wickings [c,1], K. Carpenter [f], J. Chorover [d,2], C. Rasmussen [d,2]

[a] Northern Research Station, USDA Forest Service, CAMS, L-397, 7000 East Ave, Livermore, CA 94550, USA
[b] Center for Accelerator Mass Spectrometry, Lawrence Livermore National Lab, 7000 East Ave, CA, USA
[c] Department of Natural Resources and the Environment, University of New Hampshire, 114 James Hall, Durham, NH 03824, USA
[d] Dept. of Soil, Water & Environmental Science, University of Arizona, PO Box 210038, Tucson, AZ 85721-0038, USA
[e] Department of Crop and Soil Science, Soils Division, Oregon State University, 3017 ALS Building, Corvallis, OR 97331, USA
[f] Chemical Sciences Division, PLS, Lawrence Livermore National Laboratory, 7000 East Ave, Livermore, CA 94550, USA

Received 10 December 2012; accepted in revised form 31 July 2013; available online 13 August 2013

Abstract

Solid and aqueous phase Al species are recognized to affect organic matter (OM) stabilization in forest soils. However, little is known about the dynamics of formation, composition and dissolution of organo-Al hydroxide complexes in microbially-active soil systems, where plant litter is subject to microbial decomposition in close proximity to mineral weathering reactions. We incubated gibbsite–quartz mineral mixtures in the presence of forest floor material inoculated with a native microbial consortium for periods of 5, 60 and 154 days. At each time step, samples were density separated into light (<1.6 g cm^{-3}), intermediate (1.6–2.0 g cm^{-3}), and heavy (>2.0 g cm^{-3}) fractions. The light fraction was mainly comprised of particulate organic matter, while the intermediate and heavy density fractions contained moderate and large amounts of Al-minerals, respectively. Multi-method interrogation of the fractions indicated the intermediate and heavy fractions differed both in mineral structure and organic compound composition. X-ray diffraction analysis and SEM/EDS of the mineral component of the intermediate fractions indicated some alteration of the original gibbsite structure into less crystalline Al hydroxide and possibly proto-imogolite species, whereas alteration of the gibbsite structure was not evident in the heavy fraction. DRIFT, Py–GC/MS and STXM/NEXAFS results all showed that intermediate fractions were composed mostly of lignin-derived compounds, phenolics, and polysaccharides. Heavy fraction organics were dominated by polysaccharides, and were enriched in proteins, N-bearing compounds, and lipids. The source of organics appeared to differ between the intermediate and heavy fractions. Heavy fractions were enriched in ^{13}C with lower C/N ratios relative to intermediate fractions, suggesting a microbial origin. The observed differential fractionation of organics among hydroxy-Al mineral types suggests that microbial activity superimposed with abiotic mineral-surface-mediated fractionation leads to strong density differentiation of organo-mineral complex composition even over the short time scales probed in these incubation experiments. The data highlight the strong interdependency of mineral transformation, microbial community activity, and organic matter stabilization during biodegradation.
Published by Elsevier Ltd.

* Corresponding author at: Northern Research Station, USDA Forest Service, CAMS, L-397, 7000 East Ave, Livermore, CA 94550, USA. Tel.: +1 925 422 9556; fax: +1 925 423 7884.
E-mail address: kaheckman@fs.fed.us (K. Heckman).
[1] Tel.: +1 603 862 1700.
[2] Tel.: +1 520 621 1646; fax: +1 520 621 1647.
[3] Tel.: +1 541 737 2441; fax: +1 541 737 1589.

0016-7037/$ - see front matter Published by Elsevier Ltd.
http://dx.doi.org/10.1016/j.gca.2013.07.043

1. INTRODUCTION

Aluminum hydroxides are common pedogenic minerals that can constitute a large portion of soil interfacial area, especially in acidic forest ecosystems where low pH values promote their formation and persistence. Hydroxy-Al minerals and solutes, including dissolved Al^{3+} and its hydrolysis products, are known to form strong chemical bonds with natural organic matter, thereby protecting a substantial pool of organic carbon against microbial degradation (Scheel et al., 2007, 2008; Schneider et al., 2010; Mikutta et al., 2011). However, the coupling between mineral transformation and the fractionation of organic matter–Al complexes across the potential range of Al species is not well understood, particularly in biologically active environments.

Soil Al hydroxide solids span a range in crystallinity, surface reactivity and elemental composition. Gibbsite (γ-$Al(OH)_3$) is the dominant crystalline $Al(OH)_{3(s)}$ in soils, where it occurs both as discrete particles and surface precipitates on other mineral grains (Hemingway and Sposito, 1996; Schaetzl and Anderson, 2010). When in the form of discrete particles, gibbsite is composed of plate-like layers of $Al(OH)_6$ octahedra with planar surfaces dominated by relatively unreactive hydroxyl groups (Karamalidis and Dzombak, 2010). Virtually no isomorphic substitution of divalent cations for aluminum occurs in the formation of gibbsite, yielding minerals with negligible structural charge (Huang et al., 2002). However, the edges of gibbsite particles possess under-coordinated oxygen atoms that bear pH-dependent charge and readily form electrostatic bonds with dissolved hydrophilic organics or ions in the soil solution (Johnson and Tombacz, 2002). Dissolved $Al(OH)_{x(aq)}$ species can polymerize to form poorly-crystalline solids that are similar in short-range bonding structure to gibbsite, but that lack long-range crystal order. Consequently, these poorly-crystalline Al hydroxides possess both larger specific surface area and higher pH-dependent, proton surface charge densities than gibbsite. In the presence of sufficient dissolved Si (in addition to Al), precipitation of poorly crystalline aluminosilicates such as imogolite ($SiO_2{\cdot}Al_2O_3{\cdot}2.5H_2O$) and allophane ($xSiO_2{\cdot}Al_2O_3{\cdot}yH_2O$; $x = 0.8–2$, $y \geqslant 2.5$) may occur. Similar to poorly crystalline Al hydroxides, allophane and imogolite bear an abundance of reactive surface hydroxyl groups, have high specific surface area, and large amounts of pH-dependent charge. In addition, allophane and imogolite may have isomorphic tetrahedral Al^{3+} for Si^{4+} substitutions that give rise to permanent structural charge (Harsh et al., 2002).

Differences in the physiochemical properties of these mineral phases influence their interactions with organics, resulting in variation in the types of organics bound to their surfaces and the relative strength of organic-mineral bonds. For example, the higher density of singly-coordinated oxygens on poorly crystalline mineral surfaces relative to gibbsite facilitates ligand exchange at surface hydroxyls leading to inner-sphere complexation of oxygen-containing organic moieties (e.g., phenolic, carboxyl and phosphoryl) at surface metal centers (Chorover and Amistadi, 2001; Omoike and Chorover, 2006; Mikutta et al., 2011). In comparison, the doubly coordinated hydroxyls on the gibbsite planar surface are more likely to form H-bonds or induced dipole interactions with organic sorbates. Laboratory sorption experiments indicate that poorly crystalline Al hydroxides have an affinity for phenolic acids (Huang et al., 1977), and form stable inner-sphere complexes with both phenolic and carboxylic groups (Guan et al., 2006). Reaction of dissolved monomeric Al with soluble organic matter produced Al–OM co-precipitates that were preferentially enriched in aromatic moieties and depleted in nitrogenous compounds relative to the bulk dissolved organic matter (DOM) (Scheel et al., 2007). Results of sorption experiments focusing on allophane and imogolite as the mineral substrate are less conclusive than those utilizing poorly crystalline Al hydroxides. High allophane and imogolite concentrations are often implicated as the drivers of high organic matter contents in volcanic soils (Harsh et al., 2002; Lilienfein et al., 2004), though clear evidence of preferential enrichment of certain organic compound types in association with allophanic phases has not been proven conclusively (Buurman et al., 2007). In comparison to poorly crystalline hydroxides, macrocrystalline gibbsite sorbs much smaller quantities of organic matter and the bonding mechanisms involved may be weaker (Parfitt et al., 1977; Kaiser and Guggenberger, 2000).

Though progress has been made towards understanding the formation and stability of organic–Al hydroxide complexes (Vance et al., 1996; Scheel et al., 2007; Mikutta et al., 2011; Wagai et al., 2012), many uncertainties remain, particularly regarding the microbial role in formation and dissolution of these complexes. Soil microbes produce low molecular weight organic acids (LMWOAs) as byproducts of metabolism, substrate biodegradation and cell lysis. Many LMWOAs significantly increase soil mineral dissolution rates, and can increase the total concentration of Al in equilibrium with gibbsite by as much as two to three orders of magnitude (Essington et al., 2005). DOM also affects the trajectory of secondary mineral formation through control of Al concentration and speciation (Berggren and Mulder, 1995; Wesselink et al., 1996), often decreasing the crystallinity of secondary Al hydroxide precipitates (Ng Kee Kwong and Huang, 1981; Singer and Huang, 1990; Xu et al., 2010). Whereas microbes produce many of the Al complexing organic molecules present in the soil solution, they are also strongly affected by the presence of dissolved Al. Free aqueous species in particular (e.g., Al^{3+}) are known to be toxic to soil microbes and suppress soil respiration rates even when present at micromolar concentrations (Wood, 1995; Fischer et al., 2002; Schwesig et al., 2003). In addition, sorption of organics to Al hydroxide surfaces and formation of Al–humus precipitates significantly reduce the bioavailability of those organic substrates, which also suppresses microbial activity in soils (Scheel et al., 2007; Schneider et al., 2010; Mikutta et al., 2011). In fact, recent work indicates that the formation and precipitation of Al–humus complexes, which remove OM from the bioavailable pool, may suppress biodegradation of OM to a greater degree than Al toxicity (Scheel et al., 2008).

The mechanisms regulating Al hydroxide–organic matter interactions in soils are complicated and may involve two- or three-way interactions among organic molecules,

Al hydroxides and microbial communities. To investigate the formation and composition of organic–Al hydroxide complexes in a biologically-active geochemical system relevant to soil, we incubated forest floor matter with gibbsite for periods of 5, 60 and 154 days. Different time periods were used in order to track the development of organo-mineral complexes over time (i.e., with increasing degree of biodegradation and potential gibbsite dissolution). We have reported previously (Heckman et al., 2011, 2012, Welty-Bernard et al., 2011) on time-dependent changes in microbial community composition, and water extractable organic matter (WEOM, <0.22 μm filtrate) from these incubation experiments. Analyses indicated preferential uptake of P-containing and high molar mass organics by gibbsite surfaces, as well as significant changes in microbial community composition and suppression of microbial respiration in comparison to a control treatment. Building on these previous findings, the current paper focuses on the composition of the isolated organo-mineral complexes generated in these incubations, using a suite of analytical methods optimized for solid phase interrogation including X-ray diffraction, infrared spectroscopy, pyrolysis gas chromatography–mass spectrometry (GC/MS), scanning electron microscopy–energy dispersive spectroscopy (SEM/EDS), and scanning transmission X-ray microscopy/near edge X-ray absorption fine structure (STXM/NEXAFS). The results indicate that a tight coupling between gibbsite transformation and organic matter degradation in microbially-active systems leads to the rapid (time scale of weeks) neo-formation of hydroxyl-Al–organic complexes. The experiments provide insight into the fractionation and stabilization of organic matter in pedogenic weathering products.

2. METHODS

2.1. Experimental design

Organic material from a mixed-conifer forest floor in the Santa Catalina Mountains Critical Zone Observatory (SCM-CZO) was incubated in the presence of gibbsite (with quartz as matrix) to track the formation of organo-mineral complexes throughout the degradation process. The forest floor organic material consisted of mixed Oi, Oe and Oa horizons, and was homogenized in a blender prior to use. Gibbsite and quartz grains had mean diameters of 14 μm and 211 μm, and specific surface areas of 1.32 $m^2\ g^{-1}$ and 0.03 $m^2\ g^{-1}$, respectively. Gibbsite grains exhibited long-range crystalline order and phase purity was confirmed by XRD analysis. In a 150 mL sterilized glass jar, 6.0 g gibbsite were mixed with 24.0 g quartz sand, 3.0 g homogenized forest floor material, and 1.0 mL of a forest floor derived inoculum prepared according to Wagai and Sollins (2002). Samples were incubated at 60% water holding capacity and ventilated periodically throughout the incubation in order to maintain aerobic conditions. Details of the incubation experimental design can be found in Heckman et al. (2011). In the current investigation, samples taken at 5, 60 and 154 days were examined (three statistical replicates per incubation length), to provide data pertaining to the beginning, middle and end of the incubation period. The chemical composition of soluble organic matter and metals generated in these incubations, and the ensuing changes in microbial community composition, have been published elsewhere (Heckman et al., 2011, 2012). Results of those studies that aid in interpretation of the solid phase compositional changes discussed herein are summarized when relevant in the discussion section. The solid portion of the incubation samples, composed of mineral grains and organic matter in various stages of decomposition, was oven dried at 40 °C, and then frozen at −10 °C until density separations were performed.

2.2. Density separation and isotopic characterization

After incubation, the WEOM fraction was removed by mixing the solid sample with deionized water in a 1:15 (wt:vol) ratio, shaking for 24 h and filtering at 0.22 μm. After removal of water extractable organic matter, the remaining solid portions of the incubated samples were density separated using a method modified from Strickland and Sollins (1987) and Swanston et al. (2005). Samples were composed initially of particulate organic matter, quartz grains (211 μm mean diameter), and gibbsite grains (14 μm mean diameter). The dried samples were gently broken up in a mortar and pestle then wet sieved at 53 μm to remove large particulate organic matter and quartz grains. Material less than 53 μm, composed of gibbsite grains and particulate organic matter, was added to 100 ml of sodium polytungstate (SPT) solution (Sometu; Berlin, Germany) adjusted to a density of 1.6 g cm^{-3} in 250 ml polycarbonate centrifuge tubes (Nalgene, Thermo 94 Fisher Scientific; USA). To disrupt any aggregates formed during the incubation or sample handling processes, samples were sonicated at a rate of 500 J g^{-1} soil (Rasmussen et al., 2005) using a Branson 450 Sonifier fitted with a 13 mm probe tip (Branson Ultrasonics Corporation; Danbury, CT). The rate of energy output was calibrated by measuring the change in temperature of 100 mL of DI H_2O after a 5-min treatment with ultrasonic energy (North, 1976). A schematic of the experimental setup is provided in the Supplementary materials, Supplementary Fig. 1.

After sonication, samples were left to settle for 30 min, and then centrifuged at 2000*g* for 30 min. Samples were then allowed to settle overnight. The supernatant was aspirated and filtered through a 0.22 μm polycarbonate filter. The fraction with density <1.6 g cm^{-3} (termed the *light fraction,* LF, and composed mostly of particulate organic matter) was retained but no further analyses were performed on it. The remaining material was resuspended in SPT adjusted to a density of 2.0 g cm^{-3}. The samples were centrifuged and aspirated as described above. The fraction with a density of 1.6–2.0 g cm^{-3}, termed the *intermediate fraction*, was assumed to contain a mixture of gibbsite and organic particles. The portion of sample with a density of >2.0 g cm^{-3} was termed the *heavy fraction* and was assumed to contain gibbsite particles and associated organic matter.

Isolated light, intermediate and heavy density fractions were rinsed to remove any adsorbed SPT. The intermediate fraction was rinsed using vacuum filtration, with 600 ml of 0.1 M $CaCl_2$ followed by 1000 ml of DDI water. Heavy

fractions were rinsed by repeated re-dispersion and centrifugation, also with 600 ml of 0.1 M $CaCl_2$ followed by 1000 ml of DDI water. Fractions were washed into tared beakers and dried at room temperature, under a fan to speed evaporation.

Intermediate and heavy density fractions were analyzed for %C, %N, $\delta^{13}C$ and $\delta^{15}N$ by high temperature dry combustion with an elemental analyzer (Costech Analytical Technologies, Valencia, CA, USA) coupled to a continuous-flow mass spectrometer (Finnigan Delta PlusXL, San Jose, CA, USA) at the University of Arizona Stable Isotope Laboratory.

2.3. X-ray diffraction

The intermediate and heavy density fractions were examined for alteration of gibbsite crystalline structure by X-ray diffraction (XRD). Heavy fractions were analyzed as random powder mounts. Due to their small sample size, intermediate fractions were analyzed as thin randomly-oriented powder films on a sapphire slide (CVI Melles Griot, New Mexico, USA). Fractions were scanned from 2° to 60° 2θ (0.02° step size, 3 s dwell time) on a PANalytical X'Pert PRO-MPD X-ray diffraction system (PANalytical, Almelo, AA, The Netherlands) producing Cu-Kα radiation at an accelerating potential of 45 kV and current of 40 mA, and fitted with a graphite monochromator and sealed Xenon detector. Higher resolution scans were done on the 21–26° 2θ range (0.02° step size, 20 s dwell time). Unreacted forest floor material and gibbsite were also characterized by XRD. Forest floor material was density separated at 1.6 g cm^{-3}, and both the >1.6 g cm^{-3} and bulk material were scanned. The unreacted gibbsite was separated by particle size and scans were done on the bulk material, the silt + clay fraction, and the clay fraction.

2.4. Diffuse reflectance infrared Fourier spectroscopy

Individual density fractions and a sample of unreacted gibbsite were mixed with KBr in a 1:20 w/w ratio (sample:KBr). Diffuse reflectance infrared Fourier transform (DRIFT) spectra were recorded using a Nicolet 560 Magna IR Spectrometer (Madison, WI). Ground samples were mixed with KBr, pressed gently into metal cups, and scanned over the 4000–400 cm^{-1} range. Four hundred scans were averaged for each spectrum at a resolution of 4 cm^{-1} and normalized by using pressed pure KBr as background. A manual baseline correction was applied to each spectrum to remove baseline distortions. The pure gibbsite spectrum was subtracted from that of each density fraction to isolate organic matter spectra (Chorover and Amistadi, 2001; Omoike and Chorover, 2006). Spectral analysis, including peak deconvolution and integration, was performed using the GRAMS/AI Spectroscopy Software Suite (Thermo Scientific). The relative abundance of identified functional groups was calculated as the percentage of the total area of all identified peaks. FTIR data for the WEOM fraction is also presented for comparison. Experimental conditions used for the collection of WEOM spectra were identical to those outlined above.

Peak assignments and interpretations were made in accordance with literature data (Colthup, 1950; Baes and Bloom, 1989; Gu et al., 1994; Stevenson, 1994; Gressel et al., 1995; Swift, 1996; Senesi and Loffredo, 1999; Socrates, 2001; Fu and Quan, 2006). Peaks at 3460 and 3490 cm^{-1} were assigned to metal-bound O–H stretching, most likely deriving from Al bound OH. The broad band between 3700 and 2900 cm^{-1} was assigned to the OH stretch of phenolic OH, with possible contributions from aliphatic OH and NH. The remaining peaks were assigned as follows: 2920–2855 cm^{-1} aliphatic CH, CH_2 and CH_3 stretching; 1730 cm^{-1} symmetric C=O stretch of esters; 1670–1640 cm^{-1} amide I band, C=O stretch of amides; 1605 cm^{-1} asymmetric COO^- stretch; 1510 cm^{-1} aromatic C=C stretch;1460 cm^{-1} CH_2 scissoring; 1430–1375 cm^{-1} symmetric COO^- stretch; 1275 cm^{-1} phenolic C–O(H) stretch; 1215–990 cm^{-1} C–O stretch of polysaccharides.

2.5. Pyrolysis GC/MS

40–50 mg of soil samples were first pyrolyzed at 600 °C for 20 s on a Pyroprobe 5150 (CDS Analytical Inc., Oxford, PA). Pyrolysis products were subsequently transferred to a Trace GC Ultra gas chromatograph (Thermo Fisher Scientific, Austin, TX) via a heated transfer line (300 °C). Gas chromatograph (GC) oven temperature was ramped from a starting temperature of 40–270 °C at a rate of 5° min^{-1} followed by a final ramp to 300 °C at a rate of 30° min^{-1} and compounds were separated on a fused silica capillary column (60 m, 0.25 mm i.d., 0.25 μm film thickness). Compounds were transferred to an ITQ 900 mass spectrometer (Thermo Fisher Scientific, Austin, TX) via a heated transfer line (270 °C) where they were ionized, separated in an ion trap and detected on an electron multiplier. Ion fragment patterns were used to identify compounds using the Automated Mass Spectral Deconvolution and Identification System (AMDIS, V 2.65) and the National Institute of Standards and Technology (NIST) library (Grandy et al., 2009; Wickings et al., 2011; Wickings et al., 2012). The relative abundance of identified compounds was calculated as the percentage of the total signal (area) of all identified peaks. Principal components analysis (PCA) of the compound classes was used to simplify and reduce the dimensionality of the pyrolysis GC/MS molecular carbon data set, allowing for a broad comparison of organic matter chemistry in forest floor and intermediate and heavy fractions.

2.6. Scanning electron microscopy

Soil samples were affixed to double-stick carbon tape that had been affixed to 25 mm aluminum pin mount SEM stubs. The stubs were then sputter coated with 8 nm of Iridium metal in a Cressington 208HR sputter coater. Stubs were imaged, and energy dispersive X-ray spectroscopy (EDS) elemental maps were collected using an FEI Inspect F scanning electron microscope with EDAX detector and software. A working distance of 11.5 mm and accelerating voltage of 10 kV were used for both imaging and collection of spectra. Representative images from SEM analysis are presented in Fig. 1.

2.7. Scanning transmission X-ray microscopy and near edge X-ray absorption fine structure spectroscopy (STXM/NEXAFS)

STXM/NEXAFS studies at the carbon 1s K-edge and the aluminum L-edge were performed at beamlines 5.3.2.2 (250–600 eV; Kilcoyne et al., 2003) and 5.3.2.1 (400–2500 eV; Kilcoyne et al., 2010), respectively, at the Advanced Light Source (ALS), Lawrence Berkeley National Laboratory. Intermediate fraction and heavy fraction samples were dusted on individual Si_3N_4 windows (Silson Ltd., England). To locate individual particles or microaggregates on the window, survey scans were performed below the C K-edge at 280 eV. Absorption difference maps showing the carbon distribution within particles of choice were generated by subtracting absorbance (or optical density) images below the C K-edge (280 eV) from those above (300 eV). To obtain spatially resolved C 1s spectra, stacks of images were taken at each energy increment over the C K-edge energy range (278–330 eV). C 1s stacks were collected with a dwell time of 1 ms and a spatial resolution of 40 nm. The energy spacing was chosen as follows: 0.5 eV steps from 278 to 282 eV; 0.1 eV steps from 282 to 290.1 eV; 0.5 eV steps from 290.1 to 310 eV; and 1 eV steps from 310 to 330 eV. The C 1s spectra were calibrated using the 3p Rydberg peak of gaseous CO_2 at 292.74 and 294.96 eV (Ma et al., 1991). The aXis2000 software package (Hitchcock, 2012) was used to align image stacks, generate C and Al maps, and extract NEXAFS spectra. Extracted C 1s NEXAFS spectra were normalized using the Athena software package for X-ray absorption spectroscopy (Ravel and Newville, 2005). Edge step normalization was performed using E_0 values of 290 eV across the full recorded energy range (278–330 eV). Peak assignments are included in the figure captions. The Al distribution was mapped using absorbance images below (1560 eV) and above (1570 eV) the Al L-edge energy, with a dwell time of 5 ms at a spatial resolution of 30 nm.

2.8. Statistics

The elemental composition of the fractions harvested after different lengths of incubation were compared using a two way ANOVA with fraction type (heavy vs. intermediate) and length of incubation (5, 60 and 154 days) as main effects ($n = 3$ for each treatment group). No significant differences in composition were evident among samples from different incubation lengths. Due to the lack of significant variance of the respective fractions over time, elemental compositions of intermediate fraction and heavy fraction samples were averaged over time and compared to one another using Student's t-test ($\alpha = 0.05$). Each sample harvested at a particular incubation time was treated as a statistical replicate, yielding a total of 9 replicates for each fraction type.

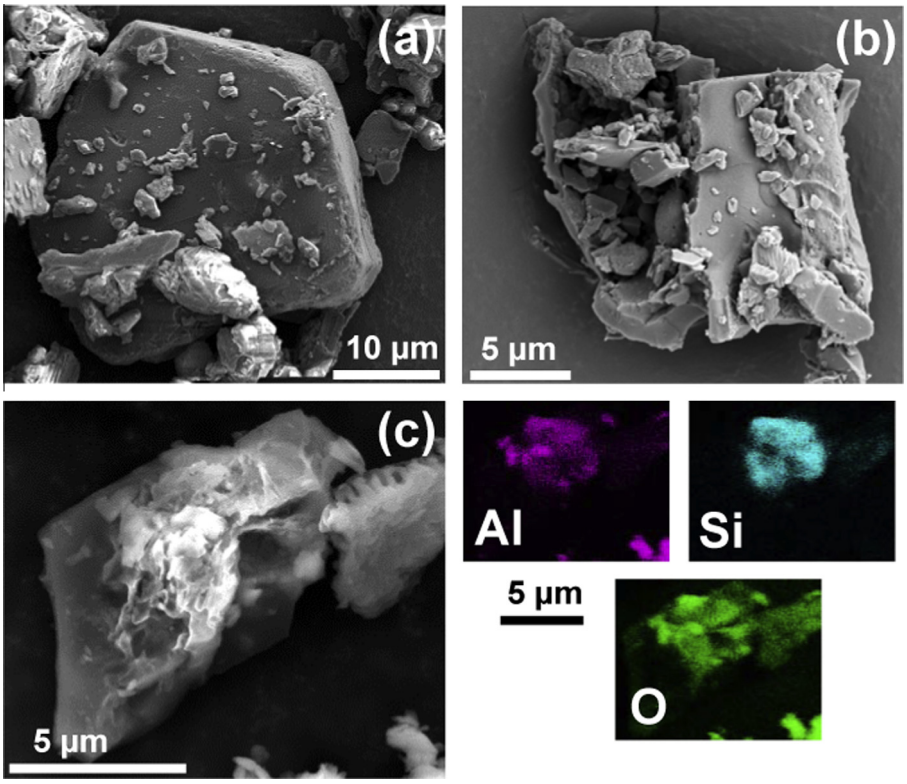

Fig. 1. SEM images of (a) heavy fraction particle after 154 days of incubation, (b) intermediate fraction particle after 154 days of incubation, and (c) intermediate fraction particle with accompanying elemental maps of aluminum, silica, and oxygen.

3. RESULTS

3.1. Elemental and isotopic analysis (%C, %N, C/N, $\delta^{13}C$, $\delta^{15}N$)

Intermediate density fractions were composed mostly of organic matter (~35% C by mass) while the heavy fractions were mostly mineral matter (~1% C by mass). C:N ratios of the intermediate fraction averaged around 30, and were significantly higher than the C:N ratio of the heavy fraction which averaged around 22 ($p < 0.0001$). Relative to intermediate fractions, heavy fraction samples were also enriched in ^{13}C ($p < 0.0001$), and depleted in ^{15}N ($p = 0.0006$). Elemental characteristics of the fractions, including ^{13}C and ^{15}N signatures, did not vary significantly over time (Table 1).

In general, decomposition leads to ^{15}N enrichment (Peterson and Fry, 1987; Dijkstra et al., 2006). The ^{15}N depletion in the heavy fraction in comparison to the intermediate fraction may be the result of nitrite and nitrate sorption to gibbsite surfaces (Mariotti et al., 1981), since gibbsite surfaces most likely carried a positive charge throughout the incubation (Karamalidis and Dzombak, 2010) and microbial communities were likely not nitrogen limited (Heckman et al., 2012).

3.2. X-ray diffraction

Full width at half maximum (FWHM) values for the main gibbsite peak in the samples were roughly 1.5 times that of the unreacted gibbsite after 154 d incubation (peak located at 20.3° 2θ, Fig. 2a). Additionally, intermediate fraction samples had low intensity broad peaks at 4.11 Å and 3.72 Å which were absent in the unreacted gibbsite, heavy fractions, and organic matter (Fig. 2b, Supplementary Fig. 2), and a large amorphous hump centered roughly at 22° 2θ.

Scans of unreacted organic matter revealed the presence of a small amount of mineral material. Organic material used in the incubation was collected from a ponderosa pine forest floor, so the presence of small amounts of mineral material is not unusual. Peaks of these mineral phases corresponded to quartz and feldspar, with smaller amounts of muscovite and kaolinite (Fig. 2b, Supplementary Fig. 2). These peaks were also evident in the heavy fraction indicating that when the solid materials were density separated, these smaller native quartz and feldspar grains were collected in the heavy fraction. FWHM values of the gibbsite peaks in the heavy fractions after 154 d of incubation were similar to those of the unreacted gibbsite.

Separation of silt and clay sized fractions of the gibbsite material indicated the presence of some amorphous clay sized particles. The low intensity broad peaks (4.11 and 3.72 Å) noted in diffractograms of the intermediate fraction samples were absent in diffractograms of both the bulk and the >1.6 g cm^{-3} fraction of forest floor (Supplementary Fig. 2).

3.3. Diffuse reflectance infrared Fourier transform (DRIFT) spectroscopy

DRIFT analysis indicated substantial differences in organic molecular composition between intermediate fractions and heavy fractions, though the respective molecular composition of the fractions did not appear to change with increasing incubation time (Figs. 3 and 4, Table 2). Bands present in spectra pertaining to the heavy fraction are consistent with enrichment in polysaccharides (C–O stretching bands between 1215 and 990 cm^{-1}) and amides (bands at 1670–1640 cm^{-1} and 1275 cm^{-1}), with smaller stretching contributions from COO^- (1430–1375 cm^{-1}) and phenolic C–O(H) (1275 cm^{-1}). DRIFT spectra for intermediate fractions show a strong polysaccharide component (C–O stretching bands between 1215–990 cm^{-1}), and significant contributions from ester-containing compounds (symmetric C=O stretching at 1730 cm^{-1}), phenolic C–O(H) stretching (1275 cm^{-1}), aromatic C=C stretching (1510 cm^{-1}), COO^- stretching (bands at 1605 cm^{-1} and 1430–1375 cm^{-1}), and amides (bands at 1670–1640 cm^{-1}) (Fig. 3b and c). Two $\nu_s(COO^-)$ bands were evident in intermediate fraction spectra (1430 and 1375 cm^{-1}), whereas only one (~1420 cm^{-1}) was present in heavy fraction spectra. For comparison, data for the WEOM fraction (from Heckman et al., 2011) are also included in Table 2. A comparison of those data shows that intermediate fraction functional group composition, as measured by infrared spectroscopy, is very similar to that of WEOM. Peaks in the intermediate fraction at 3460 and 3490 cm^{-1} are most likely representative of aluminol O–H stretching. XRD data indicated the presence of quartz

Table 1
Elemental composition of density fractions.

Density fraction	Incubation length	%C	%N	C/N	$\delta^{13}C‰$	δ15 N ‰
Forest floor	0 Days	43.2	0.9	49	−26.0	No data
Intermediate	5 Days	35.8 (±1.2)	1.2	30 (±1)	−26.2 (±0.1)	−4.5 (±0.1)
	60 Days	35.1 (±1.3)	1.1 (±0.1)	32 (±3)	−26.2	−4.2 (±0.1)
	154 Days	34.5 (±0.2)	1.3	28 (±1)	−26.4	−3.9 (±0.4)
	Average over time	35.1 (±0.4)	1.2	30 (±1)^A	−26.3 (±0.1)^A	−4.2 (±0.2)^B
Heavy	5 Days	1.3 (±0.2)	0.1	22 (±1)	−25.6	−4.9 (±0.3)
	60 Days	1.3 (±0.1)	0.1	23	−25.8 (±0.1)	−4.9 (±0.1)
	154 Days	1.4	0.1	20 (±1)	−25.7	−5 (±0.2)
	Average over time	1.3 (±0.1)	0.1	22^B	−25.7^B	−4.9^A

Numbers in parentheses are the standard error of three replicates for each incubation length, if standard error was <0.1 (or <1 for C/N values) no value is given. Letters indicate significant differences between heavy and intermediate fractions as determined by Student's t-test ($\alpha = 0.05$).

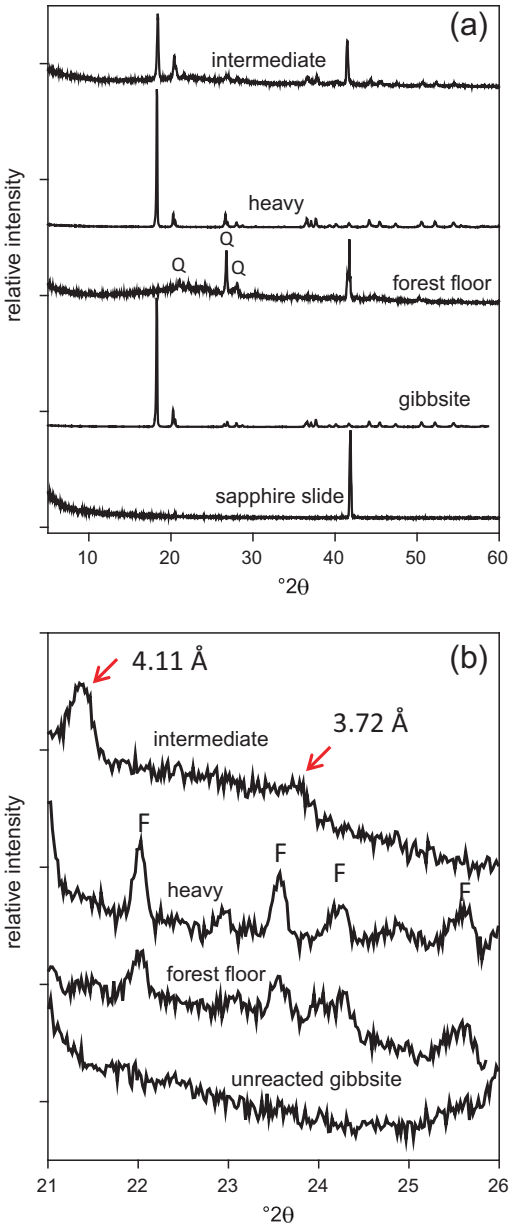

Fig. 2. X-ray diffraction patterns of density fractions. (a) from top to bottom: intermediate density fraction after 154 days of incubation, heavy density fraction after 154 days of incubation, unincubated forest floor material, unincubated gibbsite, the sapphire slide used as a mount for intermediate fraction and forest floor material. (b) High resolution scan of the 21–26 °2θ region. F denotes peaks assigned to feldspar, Q denotes peaks assigned to quartz.

and feldspar in heavy fractions, introducing the possibility of overlap between Si–O–Si stretches and carbohydrate stretches (1215–990 cm^{-1} region) in these spectra. However the symmetric Si–O band at 800 cm^{-1} was not observed in any of the spectra, indicating that the contribution of mineral vibrations aside from gibbsite was negligible.

In contrast to intermediate fraction and WEOM, spectra for heavy fraction samples indicate enrichment in amide relative to carboxylate functionality (Fig. 4a). Amide I to polysaccharide band area ratios were higher in the heavy fraction than in either the intermediate fraction or WEOM after 5 and 60 days of incubation but were similar among all fractions after 154 days (Fig. 4b).

3.4. Pyrolysis GC/MS

A total of 245 compounds were identified and grouped into the following classes with compound number in parentheses: lignin (27); lipid (35); phenol (7); N-bearing (35); unknown origin (92); polysaccharide (34); and protein (15). The most abundant compounds were pyrolysis products frequently identified in other studies (Table 3). The most common lignin-derived compounds included 4-methylguaiacol, vinylguaiacol, guaiacol, and 4-isoeugenol. The abundance of guaiacyl derived lignin reflects the dominance of this structure in coniferous forests relative to synapyl (syringyl) and *p*-hydroxycinnayl (coumaryl) and also its relative stability compared to these other lignin building blocks. The most abundant polysaccharide pyrolysis products included furfural (considered a general pyrolysis product of hexoses and pentoses) and levoglucosenone, a common pyrolysis product of cellulose (Saiz-Jimenez and De Leeuw, 1986). A greater variety of lipids was detected in this study than other recent studies (e.g. Wickings et al., 2011; Grandy et al., 2007, 2009) and of the 35 detected, 29 are estimated to be of microbial origin (i.e. a C-chain length < 20) and 6 are estimated to be originally derived from plants (Spaccini et al., 2009).

Density fraction had an overriding effect on organic matter chemistry while there was no clear effect of incubation time or fraction by time interactions (Table 4, Fig. 5). Compared to intermediate fractions, the heavy fraction had lower lignin abundance (0.098 ± 0.049 vs. 0.40 ± 0.018; $P < 0.01$); higher plant and microbial lipid abundance (0.089 ± 0.019 vs. 0.029 ± 0.003; $P < 0.01$); lower content of phenols (0.078 ± 0.011 vs. 0.104 ± 0.015; $P < 0.05$); similar abundance of N-bearing compounds (0.028 ± 0.004 vs. 0.033 ± 0.012; not significant); a trend toward higher polysaccharide abundance (0.196 ± 0.03 vs. 0.178 ± 0.005; $P < 0.1$); and substantially higher protein abundance (0.125 ± 0.022 vs. 0.042 ± 0.004; $P < 0.01$). The forest floor more closely resembled the intermediate fraction than the heavy fraction. It was dominated by lignin (relative abundance = 0.599) and unknown compounds (relative abundance of 0.193) with some phenols (relative abundance = 0.073) and polysaccharides (relative abundance = 0.085) while the relative abundance of N-bearing compounds, proteins, and lipids were all less than 0.05.

3.5. STXM/NEXAFS

C and Al maps of an aggregate taken from the intermediate fraction show an intimate association of organic matter co-aggregated within a matrix of colloidal-sized Al-bearing solids (Fig. 6A). In contrast, only one carbon-rich spot was found on the heavy fraction particle analyzed (Fig. 6B). Fig. 6C shows C NEXAFS extracted from carbon-rich regions within the intermediate fraction aggregate (spectra 1–6) and the heavy fraction particle (spectrum 7).

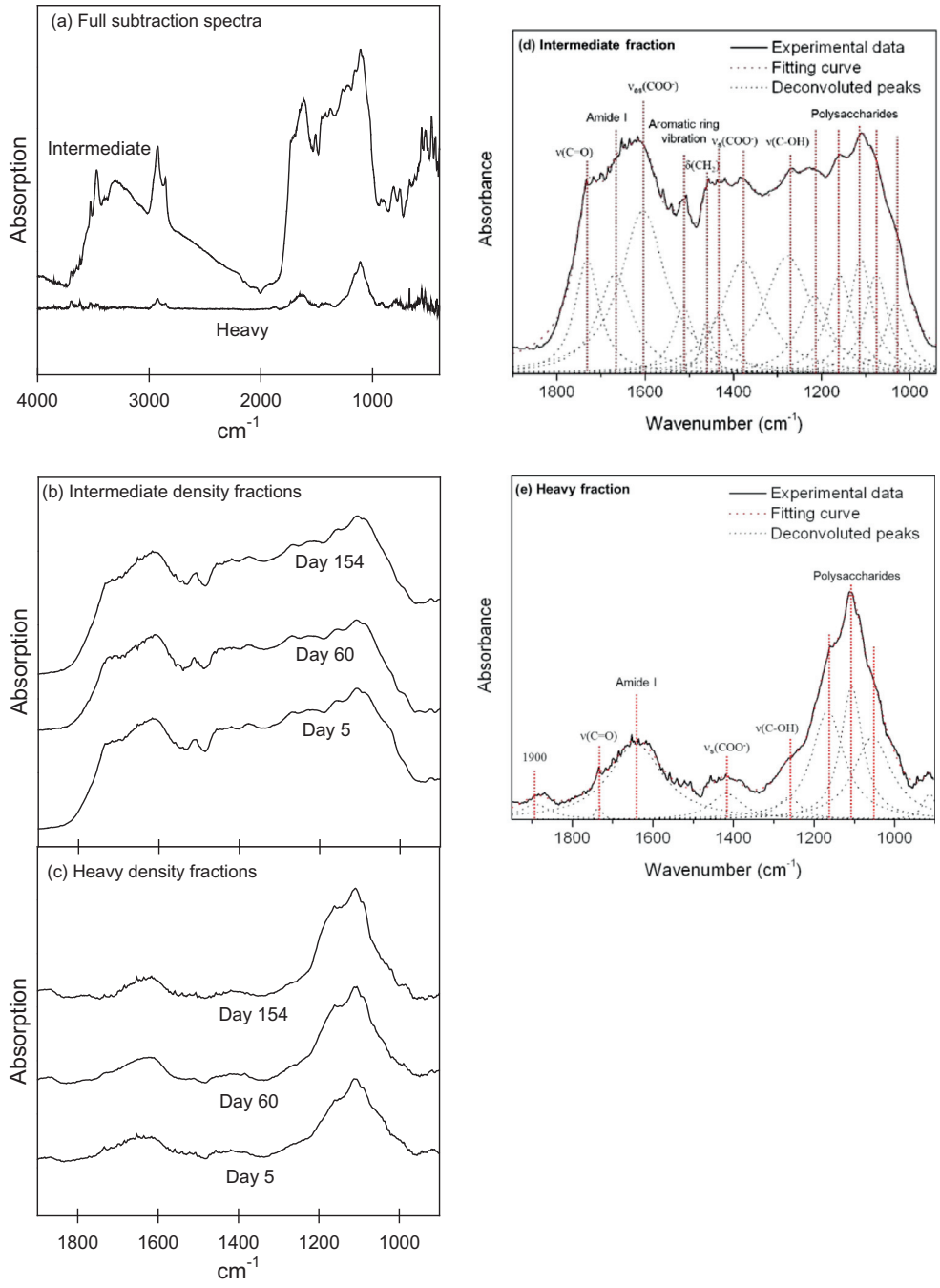

Fig. 3. DRIFT subtraction spectra of density fractions. The DRIFT spectrum of pure gibbsite was subtracted from each density fraction spectrum. (a) Full spectra from 400–4000 cm^{-1} of a representative intermediate and heavy fraction. (b) Intermediate density fractions from 900–1900 cm^{-1}. (c) Heavy density fractions from 900–1900 cm^{-1}. (d) and (e) illustrate the peak deconvolution and peak assignments tor the intermediate and heavy fractions.

C NEXAFS spectra from the intermediate fraction are very complex and show discernible peaks for aromatic C (a), phenolic C (b), aliphatic C (c), carboxyl/amide C (d), and alkyl C–O. Substantial chemical variation is seen within different regions of this aggregate: the most pronounced peaks in spectra 1, 2, 3 and 6, taken from relatively Al-rich spots, represent mainly aromatic, phenolic and carboxylic/amide C, whereas spectra 4 and 5, extracted from relatively C-rich spots, showed a more pronounced absorption band corresponding to the 1s-π^* transition of aliphatic C–H. The C NEXAFS spectrum extracted from the C-rich spot on the heavy fraction particle (region 7) showed a different chemical signature. Here a resonance of the aromatic 1s-$\pi^*_{C=C}$ transition (a) was followed by a shoulder

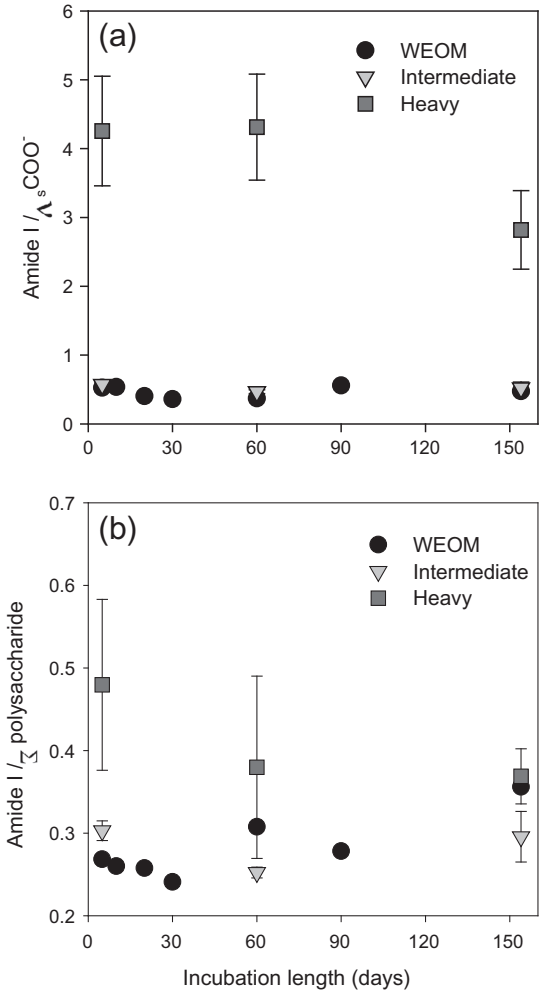

Fig. 4. Analysis of DRIFT spectra of density fractions and WEOM (water extractable organic matter). The ratio of the areas under the polysaccharide, amide 1, and the symmetric carboxyl peaks are plotted against time. (a) The ratio of the area under the Amide I band and the symmetric carboxylate stretch band are plotted against time of incubation, showing a general enrichment in amides and depletion of carboxyls in the heavy fraction in comparison to the other fractions (b) The ratio of area under the Amide I band and the sum of the polysaccharide bands is plotted against time of incubation, showing a convergence of fractions over time. For the intermediate and heavy fractions, points and error bars represent the average and standard error of 3 statistical replicates, respectively. Only one WEOM statistical replicate was tested at each sampling date.

corresponding to the aliphatic 1s-3p/σ^*_{C-H} (c) transition and a steep rise to carboxyl C–O/amide C═O transitions (d).

4. DISCUSSION

4.1. Comparison of mineral and organic components of intermediate and heavy density fractions

Distinct differences in the mineral and organic components between the intermediate and heavy fractions were observed, though these compositional differences did not change significantly with increasing time of incubation.

The heavy fraction diffractogram was virtually identical to that of unreacted gibbsite, aside from the presence of small amounts of quartz and feldspar in the heavy fractions originating from the forest floor material, consistent with a lack of gibbsite structural alteration in the heavy fraction (Fig. 2a). Conversely, the intermediate fraction mineral component showed signs of significant structural alteration relative to gibbsite and concomitant precipitation of short-range-order or amorphous phases. This is reflected in increased full width at half maximum (FWHM) values for the main gibbsite XRD peaks, and the appearance of new low intensity broad peaks (4.11 Å and 3.72) that were absent in diffractograms of the heavy fraction, unreacted gibbsite and forest floor material (Fig. 2b). Increases in FWHM values for the main gibbsite peak are indicative of a reduction in particle size, crystallinity, and/or an increase in lattice distortion (Moore and Reynolds, 1997). The new emergent peaks correspond to cell parameters of imogolite (Harsh et al., 2002), but similar peaks have been created during co-precipitation of short-range-order Al hydroxides with LMWOAs (Xu et al., 2010). The broad hump centered at 22° 2θ in the intermediate fraction samples may be wholly due to the presence of organic matter in the sample. However, the presence of amorphous minerals could also contribute to its intensity. In addition, elemental mapping (SEM/EDS) of particles from the intermediate fraction indicated the presence of an aluminum- and silica-rich precipitate on organics, another possible indication of the presence of an amorphous or poorly crystalline Al mineral phase in the intermediate fraction (Fig. 1c).

DRIFT spectra of the intermediate fractions also indicated some alteration of the gibbsite structure. Specifically, broad residual aluminol O–H stretching bands were present in the intermediate fraction DRIFT spectra even after subtraction of the unreacted gibbsite spectrum (Fig. 3a), consistent with enrichment of poorly-crystalline polymeric hydroxyl-Al solids. Broadening of aluminol peaks in Al hydroxide DRIFT spectra indicates changes in crystal structure and lattice ordering (Nguyen et al., 1991), and these same spectroscopic trends have been correlated with the relative prevalence of short-range-ordered hydroxy-Al solids co-precipitated with organic matter in a chronosequence of Hawaiian soils (Chorover et al., 2004). Poorly crystalline Al hydroxide minerals have more reactive Al–OH surface sites per unit mass than well crystallized gibbsite, enabling more intimate colloidal hetero-aggregation with organic matter (Chorover, 2012), as is nicely exemplified here in the STXM/NEXAFS data (Fig. 6).

Organic matter associated with the more crystalline gibbsite particles in the heavy fraction were of microbial origin, while that bound to the more altered mineral phases in the intermediate fraction appeared to be a mix of microbially-derived and lignin–phenol-enriched (plant-derived) material. Heavy fraction organic matter exhibited a significantly lower C/N ratio and higher ^{13}C concentrations in comparison to the forest floor material (Table 1). DRIFT spectral deconvolution of heavy fraction organic matter indicated that it was heavily enriched in amide and polysaccharide structures (Fig. 3, Table 2), a finding strongly substantiated by the protein and polysaccharide enrichments

Table 2
Relative percent contribution of individual absorbance bands to the total area under the curve of the fingerprint region (1900–900 cm-1) of DRIFT spectra.

Fraction	Absorption band	cm^{-1}	Day 5	Day 60	Day 154	Average over time
Intermediate	Ester $\nu_{as}C{=}O$	1730	7	7	7	7
	Amide I	1670	9	8 (±1)	9 (±1)	9
	$\nu_{as}(COO^-)$	1605	18 (±1)	19 (±2)	20 (±2)	19 (±1)
	aromatic ring	1510	4	4 (±1)	4 (±1)	4
	$\delta(CH_2)$	1460	2	2	2	2
	$\nu_s(COO^-)$	1430	4	4 (±1)	4 (±1)	4
	$\nu_s(COO^-)$	1375	12	13 (±1)	13 (±1)	13
	Phenolic ν(C–O(H))	1275	14 (±1)	14	13	14
	Σ polysaccharides	1030–1215	30	29 (±1)	29 (±1)	29
Heavy	Ester $\nu_{as}C{=}O$	1730	0	2 (±1)	1 (±1)	1 (±2)
	Amide I	1643	28 (±3)	24 (±1)	23 (±4)	25 (±5)
	$\nu_s(COO^-)$	1420	7 (±2)	6 (±1)	8 (±1)	7 (±3)
	Phenolic ν(C–O(H))	1275	5 (±1)	3 (±1)	4 (±1)	4 (±2)
	Σ polysaccharides	990–1160	60 (±6)	64 (±3)	64 (±4)	63 (±7)
Water extractable	Ester $\nu_{as}C{=}O$	1730	6	7	8	7
Organic matter	Amide I	1655–1640	11	10	13	11
	$\nu_{as}(COO^-)$	1580	22	21	16	21 (±1)
	$\delta(CH_2)$	1455–1445	1	0	0	0
	$\nu_s(COO^-)$	1390–1400	20	28	27	23 (±1)
	$\nu_s(COO^-)$	1385	0	0	1	0
	Σ polysaccharides	950–1235	40	34	36	38 (±1)

Intermediate and heavy: numbers in parentheses are the standard error of three replicates for each incubation length, if standard error was <0.5 no value is given. WEOM: only one spectra was examined for each incubation length.
"Average over time" values represent the average of 3 (intermediate and heavy) and seven (WEOM) sampling times.
Values in parenthesis are the standard error of 9 (intermediate and heavy) and 7 (WEOM) replicates.

measured by pyrolysis GC/MS (Table 4) and consistent with previous analyses of heavy fraction chemistry (Grandy et al., 2007). Furthermore, the heavy fraction was enriched in microbially-derived lipids in comparison to both the forest floor material and intermediate fraction and PCA analysis of the pyrolysis data indicated that heavy fraction organics bore little resemblance to the forest floor starting material (Fig. 5).

In addition to confirming the differences in organic matter molecular composition noted in DRIFT and pyrolysis GC/MS datasets, the STXM/NEXAFS analyses provided spatial understanding of the molecular distribution of this differentiated organic matter at the sub-micrometer scale. The C NEXAFS spectrum of a heavy fraction particle (Fig. 6, region 7) showed dominantly aliphatic and carboxyl/amide C components, and was most similar to spectra of microbial tissues, such as those reported for bacterial cells (Toner et al., 2006; Keiluweit et al., 2012), marine particles rich in proteins and aliphatics (Brandes et al., 2004), and organic matter associated with mineral surfaces (Lehmann et al., 2007; Kleber et al., 2011; Keiluweit et al., 2012). Aromatic C and carboxyl/amide C peaks are thought to arise from microbial proteins and DNA/RNA, while the aliphatic C is generally attributed to cell wall lipids. Though only one particle was examined, data from this spectrum strongly suggests that the organic matter associated with the heavy fraction was composed of microbial material or material that has been processed by microbial metabolism.

In comparison to the heavy fraction, DRIFT spectra of intermediate fraction samples indicated a relative enrichment of carboxylates as well as aromatic/phenolic structures (Table 2), consistent with pyrolysis data indicating enrichment in lignin-derived pyrolysates (Table 4). PCA analysis of the pyrolysis data indicated that intermediate fraction organic matter was more similar to the un-incubated forest floor material than the heavy fraction. This is likely attributable to the effective stabilization of plant-derived lignin degradation products (i.e., polyphenols) in association with poorly-crystalline mineral co-precipitates (Kramer et al., 2012). Indeed, there were significant differences between the intermediate fraction and the forest floor that indicate a higher degree of biodegradation in the intermediate fraction. Nitrogen-bearing compounds were enriched in the intermediate fraction in comparison to the un-incubated forest floor material, a difference reflected, e.g., in their respective C/N ratios (Tables 1 and 4). Lipid and polysaccharide content were also enriched in the intermediate fraction (Table 4). NEXAFS spectra indicated that the intermediate fraction organics were characteristic of biodegraded plant material; regions 1–6 in Fig. 6 has spectral characteristics resembling those of alkaline extracts of soil organic matter (Solomon et al., 2005), synthetic alkaline extracts (Hardie et al., 2009), melanoidin produced by the reaction of lysine with glucose (Brandes et al., 2004), organic matter in soil microaggregates (Kinyangi et al., 2006), water dispersible soil colloids (Schumacher et al., 2005) and aquatic dissolved organic matter

Table 3
Most abundant pyrolysates, averaged over time across all replicates.

Compound	Compound class	Fraction of total fragment abundance				
		Forest floor	Intermediate		Heavy	
		Avg.	Avg.	Std err.	Avg.	Std err.
4-Methylguaiacol	Lignin	0.137	0.056	0.007	0.000	0.000
4-Isoeugenol	Lignin	0.132	0.031	0.005	0.001	0.001
Ethylguaiacol	Lignin	0.081	0.025	0.002	0.000	0.000
Vinylguaiacol	Lignin	0.053	0.086	0.006	0.007	0.002
Guaiacol	Lignin	0.047	0.060	0.012	0.003	0.001
Vanillin	Lignin	0.041	0.026	0.003	0.006	0.002
Guaiacylacetone	Lignin	0.035	0.024	0.002	0.003	0.001
n-Undecane	Lipid	0.003	0.004	0.001	0.002	0.001
1,3-Butadiene	Lipid	0.003	0.003	0.001	0.003	0.001
n-Tridecane	Lipid	0.002	0.003	0.001	0.005	0.001
1-Hexene, 3-methyl-	Lipid	0.000	0.002	0.000	0.003	0.000
1-Heptene	Lipid	0.000	0.001	0.001	0.004	0.001
3-Decene	Lipid	0.000	0.004	0.001	0.006	0.001
n-Tricosane (C23)	Lipid	0.000	0.000	0.000	0.011	0.005
4-Methyl-phenol	Phenols	0.030	0.046	0.003	0.002	0.001
Phenol	Phenols	0.019	0.019	0.004	0.002	0.001
1-Ethyl-4-methoxy-benzene	Phenols	0.000	0.001	0.000	0.000	0.000
1,4-Dimethoxy-benzene	Phenols	0.000	0.001	0.000	0.000	0.000
4-Ethyl-phenol	Phenols	0.000	0.002	0.002	0.001	0.000
o-Xylene	Phenols	0.000	0.001	0.001	0.000	0.000
N-Hydroxy acetamide	N-Bearing	0.010	0.003	0.001	0.000	0.000
4-Amino-2(1H)-pyridinone	N-Bearing	0.005	0.005	0.001	0.000	0.000
Pyrazolo[5,1-c][1,2,4]benzotriazin-8-ol	N-Bearing	0.001	0.004	0.000	0.000	0.000
2-Amino-4-methylpyrimidine	N-Bearing	0.000	0.009	0.008	0.000	0.000
3-Methyl-1H-pyrrole	N-Bearing	0.000	0.001	0.001	0.010	0.003
3-Methyl-pyridine	N-Bearing	0.000	0.003	0.001	0.005	0.001
5-Dimethylaminopyrimidine	N-Bearing	0.000	0.000	0.000	0.004	0.002
1-(3-Hydroxy-4-methoxyphenyl)-ethanone	Unknown origin	0.043	0.013	0.005	0.000	0.000
Toluene	Unknown origin	0.024	0.036	0.005	0.059	0.008
1,2-Diethyl-benzene	Unknown origin	0.012	0.016	0.001	0.053	0.007
Pyruvaldehyde	Unknown origin	0.008	0.003	0.001	0.005	0.005
Unknown (C8H16)	Unknown origin	0.003	0.004	0.001	0.023	0.014
1-Undecanol	Unknown origin	0.001	0.003	0.000	0.004	0.001
1,3,5,7-Cyclooctatetraene	Unknown origin	0.000	0.006	0.003	0.011	0.005
2,3-Dihydro-benzofuran	Polysaccharide	0.031	0.036	0.002	0.001	0.000
Furfural	Polysaccharide	0.003	0.051	0.005	0.104	0.026
3-Furaldehyde	Polysaccharide	0.002	0.006	0.000	0.013	0.006
5-Methyl-furfural	Polysaccharide	0.001	0.002	0.000	0.041	0.014
2-Methyl-2-cyclopenten-1-one	Polysaccharide	0.000	0.006	0.001	0.022	0.004
Cyclopentanone	Polysaccharide	0.000	0.001	0.000	0.002	0.000
Levoglucosenone	Polysaccharide	0.000	0.003	0.001	0.017	0.005
Styrene	Protein	0.009	0.009	0.002	0.027	0.010
Ethylbenzene	Protein	0.005	0.007	0.001	0.027	0.007
Pyridine	Protein	0.001	0.006	0.001	0.002	0.001
Pyrrole	Protein	0.001	0.006	0.001	0.010	0.002
Pyridine	Protein	0.001	0.001	0.000	0.029	0.004
3-Methylindole	Protein	0.000	0.002	0.000	0.016	0.003
Indole	Protein	0.000	0.004	0.001	0.013	0.002

(Schumacher et al., 2006). These spectra showed particularly strong absorption in energy ranges corresponding to aromatic and phenolic C (~285 eV and ~286.5 eV, respectively) as well as carboxyl C (~288 eV), suggesting that organic matter in the intermediate fraction was mainly a heterogeneous mix of plant-derived aromatic and phenolic acids.

The molecular composition of the WEOM fraction, an important source of bioavailable C in soils (Neff and Asner, 2001), was most similar to that of the intermediate fraction (Fig. 4, Table 2). DRIFT spectral amide-to-carboxylate ratios for the WEOM fraction were nearly identical to those of the intermediate fraction over the course

Table 4
Fragment abundance by compound class for each fraction averaged across sample dates.

Compound class	Fraction of total fragment abundance		
	Forest floor	Intermediate	Heavy
Lignin	0.599	0.389 (±0.023)	0.027 (±0.008)
Lipid	0.016	0.033 (±0.007)	0.101 (±0.026)
Phenol	0.073	0.106 (±0.022)	0.064 (±0.015)
N-bearing	0.016	0.032 (±0.012)	0.026 (±0.007)
Protein	0.019	0.042 (±0.005)	0.138 (±0.036)
Polysaccharide	0.085	0.173 (±0.010)	0.241 (±0.058)
Unknown	0.193	0.223 (±0.019)	0.403 (±0.034)

Numbers in parentheses are the standard error of the mean of nine replicates.

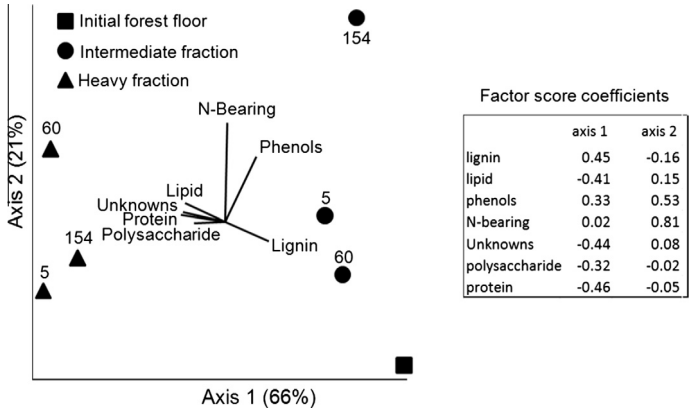

Fig. 5. Principal components analysis of compound classes in the forest floor, heavy and intermediate density fractions across time. Vector lines at center of plot indicate correlation strength of variables with axes 1 and 2. Inset shows the factor score coefficients, an indicator of the contribution each chemical class makes to the axes.

of the incubation, while amide-to-polysaccharide ratios increased significantly over time in the WEOM fraction and were very similar to those of the heavy fraction after 154 days of incubation. This suggests that while the intermediate fraction and WEOM had a similar source of forest floor-derived material throughout the incubation, there was increasing enrichment in microbially-altered compounds in the WEOM fraction over time. In general, the characteristics of the intermediate and heavy fraction organics did not change significantly over time, while those of the WEOM fraction did. Bacterial and fungal community compositions changed significantly over the course of the incubation, and these changes were correlated with changes in WEOM composition (Heckman et al., 2012). This result is important in the context of evaluating the influence of microbial community composition on organic matter degradation rates and characteristics of stabilized organic matter. It suggests that changes in microbial community composition have the largest influence on the dissolved, or easily soluble organic matter pool, but only a minor influence on the composition of mineral-bound pools. This observation is consistent with the latter being controlled more effectively by abiotic chemical reactivity of specific organic moieties for particular mineral surface functional groups.

4.2. Biotic and abiotic controls on organic matter partitioning among fractions

We propose that differences in organic matter composition between fractions arose from a combination of biotic and abiotic processes, and that organic matter released into solution during the process of microbial biodegradation was partitioned abiotically into distinct pools according to its molecular composition. Biotic processes exerted influence over organo-mineral complex formation through production of a diversity of metabolites, and through the differential colonization and dissolution of gibbsite surfaces. Together, these led to the fractionation of organic matter into pools differentially stabilized by surfaces associated with macro-crystalline gibbsite (heavy fraction) or poorly-crystalline gibbsite dissolution products (intermediate fraction).

The majority of organics found on gibbsite surfaces in the heavy fraction closely resembled microbial biomass or microbially produced compounds such as extracellular polymeric substances (EPS), and likely resulted from colonization of gibbsite surfaces by microbial communities. In a recent investigation by Mikutta et al. (2011), EPS was shown to establish strong bonds with Al hydroxide surfaces which prevented the degradation of these microbially-derived

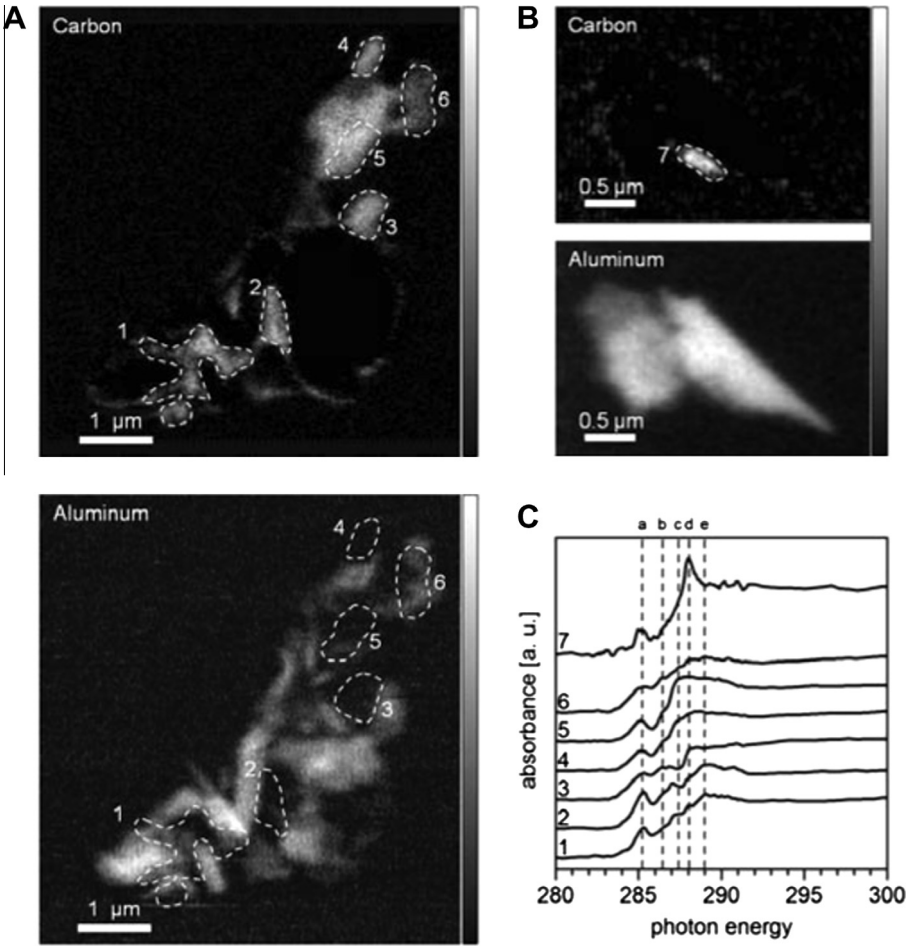

Fig. 6. STXM difference maps for carbon and aluminum of particles taken from the intermediate (A) and heavy (B) fraction (after 154 days of incubation) as well as corresponding C K-edge NEXAFS spectra for selected C-rich regions (C). C K-edge peaks in panel C are identified as (a) aromatic 1s-$\pi^*_{C=C}$ (285–285.3 eV), (b) phenolic and ketonic 1s-π^*_{C-O} (285.8–287 eV), (c) aliphatic 1s-3p/σ^*_{C-H} (287–287.6 eV), (d) carboxyl 1s-3p/σ^*_{C-O} and amide 1s-$\pi^*_{C=O}$ (288–288.5 eV), and (e) alkyl 1s-π^*_{C-O} (288.9–289.2 eV) transitions (Cody et al., 1998, 2011; Schumacher et al., 2005; Solomon et al., 2005).

substances during incubation of the EPS-Al hydroxide complexes. Oxygen containing functional groups of bacterial EPS, as well as the live bacterial cells themselves have both been shown to form covalent, inner-sphere, bonds via ligand exchange at hydroxylated mineral surfaces (Omoike and Chorover, 2006; Parikh and Chorover, 2006).

While microbial growth contributed to the accretion of organics on mineral surfaces, it also promoted the dissolution of mineral phases as evidenced by dissolved Al concentrations in the WEOM fraction that were several orders of magnitude higher than would be expected for dissolved Al in equilibrium with gibbsite (Lindsay, 1979; Heckman et al., 2011). Both microbially-produced low molecular weight organic acids and dissolved organic compounds derived from forest litter strongly increase rates of Al-bearing mineral dissolution (Pohlman and McColl, 1988; Essington et al., 2005), and the fate of dissolution products has important ramifications for organic matter stabilization in soils. Dissolved Al may directly bond with carboxyl or phenolic OH groups (Huang et al., 1977; Guan et al., 2006; Mikutta et al., 2007), with dissolved anions in solution to form, e.g., $Al(OH)_2^+$ and other species (Drabek et al., 2005), or may form short-range-order minerals prior to ripening to more crystalline solids (Hsu, 1989). Dissolved Al in the incubated microcosms of this study took a variety of forms. DRIFT spectra of the WEOM fractions showed evidence of both carboxylate–Al^{3+} bonding and the presence of $Al(OH)_x$ species, as evidenced by distortion of the carboxylate stretch band at 1385 cm^{-1} and the presence of Al–OH stretching bands at 3500 and 3530 cm^{-1}. Aluminosilicate precipitates and poorly ordered mineral phases were also noted in SEM/EDS and XRD data of intermediate fraction samples. These results indicate that dissolved Al bonded with dissolved and solid state organic matter in a variety of ways, yielding a diverse array of organo-metal and organo-mineral complexes, each with constituent-specific intermolecular affinities and, hence, preferred organic matter fractionation patterns.

Though microbial activity undoubtedly influenced the formation of organo-metal and organo-mineral complexes throughout the incubation, our data suggests that the molecular fractionation was dictated largely by abiotic factors, namely the surface chemistries of the mineral phases. Surface properties of the intermediate fraction discussed

above are known to promote the preferential binding of carboxyl and phenolic OH groups of organics through strong ligand exchange reactions (Huang et al., 1977; Chorover and Amistadi, 2001; Chorover et al., 2004; Guan et al., 2006; Schneider et al., 2010). The higher abundance of aromatic compounds, lignin-derived fragments, and phenolics in the intermediate fraction supports the idea of preferential binding of these compound types in the intermediate fraction. The presence of two carboxylate stretching bands in the intermediate fraction DRIFT spectra as opposed to only one in the heavy fraction DRIFT spectra is also suggestive of carboxylate–Al bonding in the intermediate fractions that is not readily apparent in the heavy fractions (Nakamoto, 1997; Guan et al., 2006).

In comparison, the more crystalline gibbsite surfaces of the heavy fraction accumulated organics mostly of microbial origin. The lack of distortion in the carboxylate absorption bands of DRIFT spectra suggests that ligand exchange was not the dominant bonding mechanism between organic molecules and gibbsite surfaces in the heavy fraction, and may point to electrostatic or induced dipole interactions as the main bonding mechanisms. Due to these differences in surface properties, heavy fraction mineral surfaces would be expected to sorb smaller quantities of organics (even on a surface area basis) in comparison to the intermediate fraction (Parfitt et al., 1977), and the dramatically lower %C values of heavy fraction relative to intermediate fraction samples is supportive of this concept. Gibbsite does possess edge hydroxyl groups that carry pH-dependent charge and would be suitable for inner-sphere bonding with phenolic OH and carboxyl groups, and DRIFT and pyrolysis data both indicated that these compounds were indeed present in small amounts in the heavy fraction. Organic matter accumulation in the heavy fraction may then be said to be the combined result of surface conditioning/colonization by microbial consortia and sorption of carboxyl- and phenolic-OH-bearing moieties at edge sites.

The mineralogical differences noted between heavy fraction and intermediate fraction are likely a reflection of biological weathering occurring during incubation and also the characteristics of the materials used in the incubation. The forest floor material used in the incubation contained some mineral phases identified as quartz, feldspar, muscovite and kaolinite, but may have also contained some undetectable amorphous mineral phases naturally deposited on the forest floor in the form of dust (prior to collection in the field). These amorphous mineral phases could have solubilized quickly and contributed to the formation of the amorphous and short-range-order precipitates observed in the intermediate fraction. Amorphous materials noted in the clay size fraction of the unreacted gibbsite (Supplementary Fig. 2) also likely contributed to formation of mineral phases present in the intermediate fraction. It is possible that differences in FWHM of gibbsite particles between the two fractions may not be the result of biological weathering during incubation, but may be due to variation in particle size which existed in the gibbsite material prior to incubation (gibbsite particles had an average diameter of 14 μm with a standard deviation of 11 μm as measured by laser diffraction particle size analysis). However, for this to be the case, the less crystalline particles would need to have immediately combined with organics when mixed with the forest floor material, meaning that microbial processes had little to do with the formation of bonds between gibbsite particles and organics in the intermediate fraction. But if so, this only strengthens the argument that abiotic processes play an extremely important part in the determination of soil organic matter molecular composition, and is a prime example of mineral surface properties dictating the composition of mineral-bound organic matter pools, even under conditions of active biodegradation.

It is also important to note that there was likely some desorption of organics from mineral surfaces as well as dissolution of Al-organic precipitates during both the initial WEOM extraction and the density fractionation of the incubated samples. Mikutta et al. (2011) found that up to 80% of Al-organic precipitates formed during reaction of Al^{3+} with extracellular polymeric substances dissolved when re-suspended in an Al- and organic-free solution. Given the low pH of SPT solutions (averaging around 4), it is likely there was substantial detachment of weakly bonded organics from mineral surfaces as well as dissolution of some Al-organic and amorphous mineral phases. However, despite these caveats, the composition of the organo-mineral complexes formed during this incubation experiment closely resembles that of organo-mineral complexes found in naturally formed soils (e.g., Chorover et al., 2004; Kramer et al., 2012). The microbially-based composition of the heavy fraction organics matches the composition of mineral-associated organics found in soils from a variety of environments (Poirier et al., 2005; Rasmussen et al., 2005; Grandy et al., 2007; Grandy and Neff, 2008; Sollins et al., 2009) including that of gibbsite-rich soils (Rita et al., 2011). The composition of organics in the intermediate fraction is similar to that observed for organics associated with poorly-crystalline gibbsite and short-range-order aluminosilicates in Andisols (Hatcher, 1989; Zech et al., 1994).

5. SUMMARY

Results from these simplified but biologically active systems offer an illustration of the links between microbial processes, mineral dissolution/precipitation and the stabilization of organic matter in soils. While biotic processes exerted control over the accretion of soluble organic matter and its interaction with crystalline mineral phases, thereby affecting the dissolution rate of minerals, abiotic selection processes dictated by mineral surface characteristics determined the fractionation of organic matter into well-defined pools of varying molecular composition. Furthermore, data suggest that the combined effects of these biotic and abiotic processes controlled the composition and development over time of the soluble and most bioavailable pool of organic matter which in turn had a significant influence on the decomposer community composition.

ACKNOWLEDGEMENTS

This work was supported by the National Science Foundation (DEB 0543130 and 0918718, and EAR 0724958). A portion of this

work was performed under the auspices of the U.S. Department of Energy by Lawrence Livermore National Laboratory under Contract DE-AC52-07NA27344, LLNL-JRNL-581333. Forest floor samples used in this study were collected from the Santa Catalina Mountains Critical Zone Observatory (SCM-CZO, NSF grant EAR 0724958). The authors wish to thank Dr. S. Mercer Meding (through the support of NSF EAR 0929850) for his dedicated assistance throughout this project, and Dr. C Swanston for his unflagging moral and intellectual support. The authors gratefully acknowledge A.L.D. Kilcoyne for his help and support at ALS beamlines 5.3.2.2 and 5.3.2.1 of the Advanced Light Source. The Advanced Light Source is supported by the Director, Office of Science, Office of Basic Energy Sciences, of the U.S. DOE under Contract No. DE-AC02-05CH11231. The authors extend their sincere thanks to the associate editor, Dr. Marc Norman, and two anonymous reviewers who substantially improved the quality of this manuscript.

APPENDIX A. SUPPLEMENTARY DATA

Supplementary data associated with this article can be found, in the online version, at http://dx.doi.org/10.1016/j.gca.2013.07.043.

REFERENCES

Baes A. U. and Bloom P. R. (1989) Diffuse Reflectance and Transmission Fourier Transform Infrared Spectroscopy of Humic and Fulvic Acids. *Soil Sci. Am. J.* **53**, 695–700.

Berggren D. and Mulder J. (1995) The role of organic matter in controlling aluminum solubility in acidic mineral soil horizons. *Geochim. Cosmochim. Acta* **59**, 4167–4180.

Brandes J. A., Lee C., Wakeham S., Peterson M., Jacobson C., Wirick S. and Cody G. (2004) Examining marine particulate organic matter at sub-micron scales using scanning transmission X-ray microscopy and carbon X-ray absorption near edge structure spectroscopy. *Mar. Chem.* **92**, 107–121.

Buurman P., Peterse F. and Almendros Martin G. (2007) Soil organic matter chemistry in allophanic soils: a pyrolysis–GC/MS study of a Costa Rican Anodosol Catena. *Euro. J. Soil Sci.* **58**, 1330–1347.

Chorover J. (2012) Impact of soil physicochemical and biological reactions on transport of nutrients and pollutants in the critical zone. In *Handbook of Soil Science: Resource Management and Environmental Impacts* (ed. P. M. Huang). Academic Press, NY, pp. 10–11, 10–35.

Chorover J. and Amistadi M. K. (2001) Reaction of forest floor organic matter at goethite, birnessite and smectite surfaces. *Geochim. Cosmochim. Acta* **65**, 95–109.

Chorover J., Amistadi M. K. and Chadwick O. A. (2004) Surface charge evolution of mineral-organic complexes during pedogenesis in Hawaiian basalt. *Geochim. Cosmochim. Acta* **68**, 4859–4876.

Cody G. D., Ade H., Wirick S., Mitchell G. D. and Davis A. (1998) Determination of chemical- structural changes in vitrinite accompanying luminescence alteration using C-NEXAFS analysis. *Org. Geochem.* **28**, 441–455.

Cody G. D., Gupta N. S., Briggs D. E. G., Kilcoyne A. L. D., Summons R. E., Kenig F., Plotnick R. E. and Scott A. C. (2011) Molecular signature of chitin–protein complex in Paleozoic arthropods. *Geology* **39**, 255–258.

Colthup N. B. (1950) Spectra-structure correlations in the infra-red region. *J. Opt. Soc. Am.* **40**(6), 397–400.

Dijkstra P., Ishizu A., Doucett R., Hart S. C., Schwartz E., Menyailo O. V. and Hungate B. A. (2006) ^{13}C and ^{15}N natural abundance of the soil microbial biomass. *Soil Bio. Biochem.* **38**, 3257–3266.

Drabek O., Mladkova L., Boruvka L., Szakova J., Nikodem A. and Nemeek K. (2005) Comparison of water-soluble and exchangeable forms of Al in acid forest soils. *J. Inorg. Biochem.* **99**, 1788–1795.

Essington M. E., Nelson J. B. and Holden W. L. (2005) Gibbsite and goethite solubility: the influence of 2-ketogluconate and citrate. *Soil Sci. Soc. Am. J.* **69**, 996–1008.

Fischer J., Quintmeier A., Gansel S., Sabados V. and Friedrich C. G. (2002) Inducible aluminum resistance of *Acidiphilium cryptum* and aluminum tolerance of other acidophilic bacteria. *Arch. Microbiol.* **178**, 554–558.

Fu H. and Quan X. (2006) Complexes of fulvic acid on the surface of hematite, goethite, and akaganeite: FTIR observation. *Chemosphere* **63**, 403–410.

Grandy A. S. and Neff J. C. (2008) Molecular C dynamics downstream: the biochemical decomposition sequence and its impact on soil organic matter structure and function. *Sci. Total Environ.* **404**, 297–307.

Gressel N., McGrath A. E., McColl J. G. and Powers R. F. (1995) Spectroscopy of aqueous extracts of forest litter. I: suitability of methods. *Soil Sci. Soc. Am. J.* **59**, 1715–1723.

Gu B., Schmitt J., Chen Z., Liang L. and McCarthy J. F. (1994) Adsorption and desorption of natural organic matter on iron oxide: mechanisms and models. *Environ. Sci. Technol.* **28**, 38–46.

Guan X.-H., Shang C. and Chen G.-H. (2006) ATR-FTIR investigation of the role of phenolic groups in the interaction of some NOM model compounds with aluminum hydroxide. *Chemosphere* **65**, 2074–2081.

Grandy A. S., Neff J. C. and Weintraub M. N. (2007) Carbon structure and enzyme activities in alpine and forest ecosystems. *Soil Biol. Biochem.* **39**, 2701–2711.

Grandy A. S., Strickland M. S., Lauber C. L., Bradford M. A. and Fierer N. (2009) The influence of microbial communities, management, and soil texture on soil organic matter chemistry. *Geoderma* **150**, 278–286.

Hardie A. G., Dynes J. J., Kozak L. M. and Huang P. M. (2009) The role of glucose in abiotic humification pathways as catalyzed by birnessite. *J. Mol. Catal. A. Chem.* **308**, 114–126.

Harsh J., Chorover J. and Nizeyimana E. (2002) Allophane and imogolite. In *Soil Mineralogy with Environmental Applications* (eds. J. B. Dixon and D. G. Schulze). Soil Science Society of America Inc., Madison, Wisconsin, USA, pp. 291–322.

Hatcher P. G. (1989) The chemical structure of highly aromatic humic acids in three volcanic ash soils as determined by dipolar dephasing NMR studies. *Geochim. Cosmochim. Acta* **53**, 125–130.

Heckman K., Vazquez-Ortega A., Gao X., Chorover J. and Rasmussen C. (2011) Changes in water extractable organic matter during incubation of forest floor material in the presence of quartz, goethite and gibbsite surfaces. *Geochim. Cosmochim. Acta* **75**, 4295–4309.

Heckman K., Welty-Bernard A., Vazquez-Ortega A., Schwartz E., Chorover J. and Rasmussen C. (2012) The influence of goethite and gibbsite on soluble nutrient dynamics and microbial community composition. *Biogeochemistry*. http://dx.doi.org/10.1007/s10533-012-9715-2.

Hemingway B. S. and Sposito G. (1996) Inorganic aluminum-bearing solid phases. In *The Environmental Chemistry of Aluminum* (ed. G. Sposito). Lewis Publishers, Boca Raton, FL, pp. 169–220.

Hitchcock A. P. (2012). Available at: <http://unicorn.mcmaster.ca/aXis2000.html>.

Huang P. M., Wang T. S. C., Wang M. K., Wu M. H. and Hsu N. W. (1977) Retention of pheolic acids by noncrystalline hydroxyl-aluminum and -iron compounds and clay minerals of soils. *Soil Sci.* **123**, 213–219.

Huang P. M., Wang M. K. and Schulze D. G. (2002) Aluminum Hydroxides. In *Soil Mineralogy with Environmental Applications* (eds. J. B. Dixon and D. G. Schulze). Soil Science Society of America, Inc., Madison, WI, USA, pp. 261–290.

Hsu P. H. (1989) Aluminum hydroxides and oxyhydroxides. In *Minerals in Soil Environments* (eds. J. B. Dixon and S. B. Weed). Soil Science Society of America, Madison, WI, USA, pp. 331–378.

Johnson C. T. and Tombacz E. (2002) Surface chemistry of soil minerals. In *Soil Mineralogy with Environmental Applications. SSSA Book Ser. 7* (eds. J. B. Dixon and D. G. Schulze). SSSA, Madison, WI, pp. 37–68.

Kaiser K. and Guggenberger G. (2000) The role of DOM sorption to mineral surfaces in the preservation of organic matter in soils. *Org. Geochem.* **31**, 711–725.

Karamalidis A. K. and Dzombak D. A. (2010) *Surface complexation modeling: gibbsite*. John Wiley & Sons, Inc., Hoboken, New Jersey, USA.

Keiluweit M., Bougoure J. J., Zeglin L. H., Myrold D. D., Weber P. K., Pett-Ridge J., Kleber M. and Nico P. (2012) Nano-scale investigation of the association of microbial nitrogen residues with iron (hydr)oxides in a forest soil O-horizon. *Geochim. Cosmochim. Acta* **95**, 213–226.

Kilcoyne A. L. D., Ade H., Attwood D., Hitchcock A. P., McKean P., Mitchell G. E., Monteiro P., Tyliszczak T. and Warwick T. (2010) A new Scanning Transmission X-ray Microscope at the ALS for operation up to 2500 eV. *AIP Conf. Proc.* **1234**, 459–462.

Kilcoyne A. L. D., Tyliszczak T., Steele W. F., Fakra S., Hitchcock P., Franck K., Anderson E., Harteneck B., Rightor E. G., Mitchell G. E., Hitchcock A. P., Yang L., Warwick T. and Ade H. (2003) Interferometer controlled scanning transmission X-ray microscopes at the advanced light source. *J. Synchrotron Radiat.* **10**, LBNL-53202.

Kinyangi J., Solomon D., Liang B. I., Lerotic M., Wirick S. and Lehmann J. (2006) Nanoscale biogeocomplexity of the organo-mineral assemblage in soil: application of STXM microscopy and C 1s-NEXAFS spectroscopy. *Soil Sci. Soc. Am. J.* **70**, 1708–1718.

Kleber M., Nico P. S., Plante A., Filley T., Kramer M., Swanston C. and Sollins P. (2011) Old and stable soil organic matter is not necessarily chemically recalcitrant: implications for modeling concepts and temperature. *Global Change Biol.* **17**, 1097–1107.

Kramer M., Sanderman J., Chadwick O. A., Chorover J. and Vitousek P. M. (2012) Long-term carbon storage through retention of dissolved aromatic acids by reactive particles in soil. *Global Change Biol.* **18**, 2594–2605. http://dx.doi.org/10.1111/j.1365-2486.2012.02681.x.

Lehmann J., Kinyangi J. and Solomon D. (2007) Organic matter stabilization in soil micro-aggregates: implications from spatial heterogeneity of organic carbon contents and carbon forms. *Biogeochemistry* **85**, 45–57.

Lilienfein J., Qualls R. G., Uselman S. M. and Bridgham S. D. (2004) Adsorption of dissolved organic carbon and nitrogen in soils of a weathering chronosequence. *Soil Sci. Soc. Am. J.* **68**, 292–305.

Lindsay W. L. (1979) *Chemical Equilibria in Soils*. John Wiley & Sons, New York.

Ma Y., Chen C. T., Meigs G., Randall K. and Sette F. (1991) High-resolution K-shell photoabsorption measurements of simple molecules. *Phys. Rev. A* **44**, 1848–1858.

Mariotti A., Germon J. C., Huber P., Kaiser P., Letolle R., Tardieux A. and Tardieux P. (1981) Experimental determination of nitrogen kinetic isotope fractionation: some principles; illustration for the denitrification and nitrification processes. *Plant Soil* **62**, 413–430.

Mikutta R., Mikutta C., Kalbiz K., Scheel T., Kaiser K. and Jahn R. (2007) Biodegradation of forest floor organic matter bound to minerals via different binding mechanisms. *Geochim. Cosmochim. Acta* **71**, 2569–2590.

Mikutta R., Zang U., Chorover J., Haumaier L. and Kalbitz K. (2011) Stabilization of extracellular polymeric substances (*Bacillus subtilis*) by adsorption to and coprecipitation with Al forms. *Geocim. Cosmochim. Acta* **75**, 3135–3154.

Moore D. M. and Reynolds, Jr., R. C. (1997) *X-Ray diffraction and the identification and analysis of clay minerals*, second ed. Oxford University Press, New York.

Nakamoto K. (1997) *Infrared and Raman Spectra of Inorganic and Coordination Compounds*. John Wiley & Sons, New York.

Neff J. C. and Asner G. P. (2001) Dissolved organic carbon in terrestrial ecosystems: synthesis and a model. *Ecosystems* **4**, 29–48.

Ng Kee Kwong K. F. and Huang P. M. (1981) Comparison of the influence of tannic acid and selected low-molecular-weight organic acids on precipitation products of aluminium. *Geoderma* **26**, 179–193.

Nguyen T. T., Janik L. J. and Raupach M. (1991) Diffuse Reflectance Infrared Fourier Transform (DRIFT) spectroscopy in soil studies. *Aust. J. Soil Res.* **29**, 49–67.

North P. F. (1976) Towards an absolute measurement of soil structural stability using ultrasound. *Soil Sci. Soc. Am. J.* **27**, 451–459.

Omoike A. and Chorover J. (2006) Adsorption to goethite of extracellular polymeric substances from Bacillus subtilis. *Geochim. Cosmochim. Acta* **70**, 827–838.

Parfitt R. L., Fraser A. R. and Farmer V. C. (1977) Adsorption on hydrous oxides. III. Fulvic and humic acid on goethite, gibbsite and imogolite. *Eur. J. Soil Sci.* **28**, 289–296.

Parikh S. J. and Chorover J. (2006) ATR-FTIR reveals bond formation during bacterial adhesion to Fe oxide. *Langmuir* **22**, 8492–8500.

Peterson B. J. and Fry B. (1987) Stable isotopes in ecosystem studies. *Annu. Rev. Ecol. Syst.* **18**, 293–320.

Pohlman A. A. and McColl J. G. (1988) Soluble organics from forest litter and their role in metal dissolution. *Soil Sci. Soc. Am. J.* **52**, 265–271.

Poirier N., Sohi S. P., Guant J. L., Mahieu N., Randall E. W. and Powlson D. S., et al. (2005) The chemical composition of measurable soil organic matter pools. *Org. Geochem.* **36**, 1174–1189.

Rasmussen C., Torn M. S. and Southard R. J. (2005) Mineral assemblage and aggregates control carbon dynamics in a California conifer forest. *Soil Sci. Soc. Am. J.* **69**, 1711–1721.

Ravel B. and Newville M. (2005) ATHENA, ARTEMIS, HEPHAESTUS: data analysis for X-ray absorption spectroscopy using IFEFFIT. *J. Synchrotron Radiat.* **12**, 537–541.

Rita J. C. O., Gama-Rodrigues E. F., Gama-Rodrigues A. C., Polidoro J. C., Machado R. C. R. and Baligar V. C. (2011) C and N Content in Density Fractions of Whole Soil and Soil Size Fraction Under Cacao Agroforestry Systems and Natural Forest in Bahia, Brazil. *Environ. Manage.*. http://dx.doi.org/10.1007/s00267-011-9642-3.

Saiz-Jimenez C. and De Leeuw J. W. (1986) Chemical characterization of soil organic matter fractions by analytical pyrolysis–gas chromatography–mass spectrometry. *J. Anal. Appl. Pyrolysis* **9**, 99–119.

Schaetzl R. J., and Anderson S. (Eds.) (2010) *Soils: Genesis and Geomorphology*, Cambridge University Press, New York.

Scheel T., Dörfler C. and Kalbitz K. (2007) Precipitation of dissolved organic matter by aluminum stabilizes carbon in acidic forest soils. *Soil Sci. Soc. Am. J.* **71**, 64–74.

Scheel T., Jansen B., van Wijk A. J., Verstraten J. M. and Kalbitz K. (2008) Stabilization of dissolved organic matter by aluminium: a toxic effect or stabilization through precipitation?. *Eur. J. Soil Sci.* **59** 1122–1132.

Schneider M. P. W., Scheel T., Mikutta R., van Hees P., Kaiser K. and Kalbitz K. (2010) Sorptive stabilization of organic matter by amorphous Al hydroxide. *Geochim. Cosmochim. Acta* **74**, 1606–1619.

Schumacher M., Christl I., Scheinost A. C., Jacobsen C. and Kretzschmar R. (2005) Chemical heterogeneity of organic soil colloids investigated by scanning transmission X-ray microscopy and C-1s NEXAFS micro-spectroscopy. *Environ. Sci. Technol.* **39**, 9094–9100.

Schumacher M., Christl I., Vogt R. D., Barmettler K., Jacobsen C. and Kretzschmar R. (2006) Chemical composition of aquatic dissolved organic matter in five boreal forest catchments sampled in spring and fall seasons. *Biogeochemistry* **80**, 263–275.

Schwesig D., Kalbitz K. and Matzner E. (2003) Effects of aluminium on the mineralization of dissolved organic carbon derived from forest floors. *Eur. J. Soil Sci.* **54**, 311–322.

Senesi N. and Loffredo E. (1999) The chemistry of soil organic matter. In *Soil Physical Chemistry* (ed. D. L. Sparks), second ed. CRD Press LLC, New York, pp. 239–370.

Singer A. and Huang P. M. (1990) Effects of humic acid on the crystallization of aluminum hydroxides. *Clays Clay Miner.* **38**, 47–52.

Socrates G. (2001) *Infrared and Raman Characteristic Group Frequencies: Tables and Charts*, third ed. John Wiley & Sons, Ltd., New York.

Sollins P., Kramer M. G., Swanston C., Lajtha K., Filley T., Aufdenkampe A. K., Wagai R. and Bowden R. D. (2009) Sequential density fractionation across soils of contrasting mineralogy: evidence for both microbial- and mineral-controlled organic matter stabilization. *Biogeochemistry* **96**, 209–231.

Solomon D., Lehmann J., Kinyangi J., Liang B. and Schäfer T. (2005) Carbon K-edge NEXAFS and FTIR-ATR spectroscopic investigation of organic carbon speciation in soils. *Soil Sci. Soc. Am. J.* **69**, 107–119.

Spaccini R., Sannino D., Piccolo A. and Fagnano M. (2009) Molecular changes in organic matter of a compost amended soil. *Eur. J. Soil Sci* **60**, 287–296.

Stevenson F. J. (1994) *Humus Chemistry—Genesis, Composition, Reactions*, 2nd Ed. Wiley, New York.

Strickland T. C. and Sollins P. (1987) Improved method for separating light-fraction and heavy-fraction organic material from soil. *Soil Sci. Soc. Am. J.* **51**, 1390–1393.

Swanston C., Torn M., Hanson P., Southon J., Garten C., Hanlon E. M. and Ganio L. (2005) Initial characterization of processes of soil carbon stabilization using forest stand-level radiocarbon enrichment. *Geoderma* **128**, 52–62.

Swift R. S. (1996) Organic matter characterization. In *Methods of Soil Analysis: Part 3, Chemical Methods, SSSA Book Series 5* (ed. D. L. Sparks et al.). Soil Science Society of America, Madison, WI, pp. 1018–1020.

Toner B., Manceau A., Webb S. and Sposito G. (2006) Zinc sorption to biogenic hexagonal-birnessite particles within a hydrated bacterial biofilm. *Geochim. Cosmochim. Acta* **70**, 27–43.

Vance G. F., Stevenson F. J. and Sikora F. J. (1996) Environmental chemistry of aluminum–organic complexes. In *The Environmental Chemistry of Aluminum* (ed. G. Sposito). Lewis Publishers, Boca Raton, FL, pp. 169–220.

Wagai R. and Sollins P. (2002) Biodegradation and regeneration of water-soluble carbon in a forest soil: leaching column study. *Biol. Fert. Soils* **35**, 18–26.

Wagai R., Mayer L. M., Kitayama K. and Shirato Y. (2012) Association of organic matter with iron and aluminum across a range of soils determined via selective dissolution techniques coupled with dissolved nitrogen analysis. *Biogeochem.* **112**, 95–109.

Welty-Bernard A. T., Heckman K., Vazquez A., Rasmussen C., Chorover J. and Schwartz E. (2011) Microbial composition in decomposing pine litter shifts in response to common soil secondary minerals. Abstract B51G-0483 presented at 2011 Fall Meeting, AGU, San Francisco, Calif., 5–9 Dec.

Wesselink L. G., Van Breemen N., Mulder J. and Janssen P. H. (1996) A simple model of soil organic matter complexation to predict the solubility of aluminium in acid forest soils. *Eur. J. Soil Sci.* **47**, 373–384.

Wickings K., Grandy A. S., Reed S. and Cleveland C. (2011) Management intensity alters decomposition via biological pathways. *Biogeochemistry* **104**, 365–379.

Wickings K., Grandy A. S., Reed S. and Cleveland C. (2012) The origin of litter chemical complexity during decomposition. *Ecol. Lett.* **15**, 1180–1188.

Wood M. (1995) A mechanism of aluminum toxicity to soil bacteria and possible ecological implications. *Plant Soil* **171**, 63–69.

Xu R. K., Hu Y. F., Dynes J. J., Zhao A. Z., Blyth R. I. R., Kozak L. M. and Huang P. M. (2010) Coordination nature of aluminum (oxy)hydroxides formed under the influence of low molecular weight organic acids and a soil humic acid studied by X-ray absorption spectroscopy. *Geochim. Cosmochim. Acta* **74**, 6422–6435.

Zech W., Haumaier L., Guggenberger G., Gil-Sotres F. and Arai S. (1994) Changes in carbon species distribution of humic substances with depth in mineral soils of various origin. In *Humic Substances in the Global Environment and Implications on Human Health* (eds. N. Senesi and T. M. Miano). Elsevier, Amsterdam, pp. 445–450.

Associate editor: Christopher John Daughney